Reducing Operating Temperature in Photovoltaic Modules

Timothy J. Silverman, Michael G. Deceglie, Indra Subedi, Nikolas J. Podraza, Ian M. Slauch, Vivian E. Ferry, and Ingrid Repins

Abstract—**Reducing the operating temperature of photovoltaic modules increases their efficiency and lifetime. This can be achieved by reducing the production of waste heat or by improving the rejection of waste heat. We tested, using a combination of simulation and experiment, several thermal modifications in each category. To predict operating temperature and energy yield changes in response to changes to the module, we implemented a physics-based transient simulation framework based almost entirely on measured properties. The most effective thermal modifications reduced the production of waste heat by reflecting unusable light from the cell or the module. Consistent with previous results and verified in this work through year-long simulations, the ideal reflector resulted in an annual irradiance-weighted temperature reduction of 3.8 K for crystalline silicon (c-Si). Our results illustrate that more realistic reflector concepts must balance detrimental optical effects with the intended thermal effects to realize the optimal energy production advantage. Methods improving thermal conductivity or back-side emissivity showed only modest improvements of less than 1 K. We also studied a GaAs module, which uses high-efficiency and high-subbandgap reflectivity to operate at an annual irradiance-weighted temperature 12 K cooler than that of a c-Si module under the same conditions.**

Index Terms—**Computer simulation, optics, photovoltaic cells, photovoltaic systems, ray tracing, solar energy, solar panels, thermal conductivity, thermal management.**

T. J. Silverman, M. G. Deceglie, and I. Repins are with the National Center for Photovoltaics, National Renewable Energy Laboratory, Golden, CO 80401 USA (e-mail: timothy.silverman@nrel.gov; michael.deceglie@nrel.gov; ingrid.repins@nrel.gov).

I. Subedi and N. J. Podraza are with the Department of Physics and Astronomy and the Wright Center for Photovoltaics Innovation and Commercialization, University of Toledo, Toledo, OH 43606 USA (e-mail: Indra.Subedi@rockets.utoledo.edu; Nikolas.Podraza@utoledo.edu).

I. M. Slauch and V. E. Ferry are with the Department of Chemical Engineering and Materials Science, University of Minnesota, Minneapolis, MN 55455 USA (e-mail: slauc001@umn.edu; veferry@umn.edu).

Color versions of one or more of the figures in this paper are available online at http://ieeexplore.ieee.org.

Digital Object Identifier 10.1109/JPHOTOV.2017.2779842

I. Introduction

ALL common types of solar cells lose efficiency with increasing temperature. Reducing a solar cell's temperature is one of the most effective ways of increasing its energy output. When they are deployed outdoors, solar cells are interconnected and packaged in a module [1]. Because many of the module's degradation mechanisms are thermally activated, reduced operating temperature is also an effective way of increasing the lifetime of a photovoltaic (PV) module [2]. A wide range of techniques have been investigated for cooling PV modules [3]–[7].

PV modules operate above the ambient temperature because they convert some of the incident sunlight into waste heat, for instance, due to absorption of subbandgap light or thermalization of carriers to the band edge. This production of waste heat is balanced by the rejection of heat, mainly by convection and radiation. This suggests two classes of strategies for reducing operating temperature: 1) reduction of waste heat production and 2) improvement of waste heat rejection. In this work, we use a combination of computational modeling and outdoor experimentation to quantify the effect of several thermal modifications in each category. We do not consider dynamic temperature-reduction strategies, such as phase-change materials, desiccants, or active cooling by artificial forced convection. We also do not consider modifications to the forced and free convection occurring naturally outdoors.

II. Method

We studied the effect of several thermal modifications. For each one, we performed either computer simulations, outdoor experiments, or both. Two types of computer simulation were used: a transient simulation for up to a full year in Golden, CO, USA, and a steady-state simulation at fixed irradiance. Both are described in more detail in the following.

We used two metrics to compare the modifications. Irradiance-weighted mean cell temperature rise above ambient, ΔT_w, gives a way of comparing operating temperature with emphasis on times when the production of energy is high

$$\Delta T_w = \frac{\sum_t \left(T_{\text{module}} - T_{\text{ambient}} \right) G_{\text{POA}}}{\sum_t G_{\text{POA}}}$$

where G_{POA} is plane-of-array irradiance and $\sum_t$ indicates a summation over time. When a steady-state simulation is used, ΔT_w simplifies to the temperature rise above ambient for the conditions of the simulation. We always made relative

comparisons of the value of ΔT_w between a baseline module (see Section II-A) and a test module. The second metric we used for comparing the modifications was cumulative dc energy output, E_{DC}, which we also evaluated in comparison with a baseline module. In the case of the GaAs module, because of the different size and technology of the baseline and test modules, the energy produced by each module was normalized to that module's performance at standard test conditions (STC).

For modifications simulated with the transient model, we decomposed the total energy benefit into "thermal" and "other" components. The total energy benefit was calculated as the ratio of the additional energy generated by the modified module to the total energy generated by the baseline module for the full simulation period. The thermal benefit was calculated using

$$\sum_t P_{\text{baseline}} \gamma (T_{\text{modified}} - T_{\text{baseline}})$$

where P_{baseline} is the operating power of the baseline module, γ is the power temperature coefficient, T_{modified} is the operating temperature of the modified module, T_{baseline} is the operating temperature of the baseline module, and the sum is taken over the entire simulated time series. The "other" energy benefits include increased efficiency, photocurrent, or smaller magnitude temperature coefficient.

For calculating the comparison metrics on experimental data, we considered only conditions when the module was free of snow and when irradiance exceeded $50 \, \text{W} \cdot \text{m}^{-2}$. When only simulation results were available, we compared cell temperature. For the experiment, described below, where a reflective coating was applied to the module's back surface, we used cell temperature derived from V_{oc} and irradiance. Otherwise, we compared measured and simulated module back surface temperatures.

A. Baseline Modules

Each temperature reduction was quantified in relation to a baseline module. We used different types of baseline modules in simulations to ensure a fair comparison of each modification and in experiments depending on data availability. In the following descriptions, efficiency refers to the module's measured STC efficiency during our tests and/or simulations.

Module A was a simulated 17.1% efficient crystalline silicon module with conventional packaging materials: glass front, ethylene vinyl acetate (EVA) encapsulation, and white polymer backsheet. To simplify the geometry for many simulations of an entire year of service, module A had no frame and had a uniform layer representing the cells.

Module B was a simulated crystalline silicon module based on module A, but with an aluminum frame and individual cells. It represented a 2-D cross section through a module with six columns of cells. Module B was used only for steady-state simulations.

Module C was a real copper indium gallium diselenide (CIGS) module with glass on both the front and back surfaces. This module was made in 2014 and was the only module with an antireflective coating on the front surface of the glass.
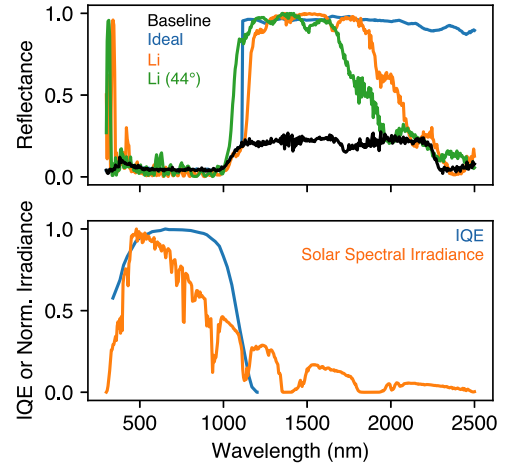

Fig. 1. Total reflectance (top) for various simulated modules is shown with the normalized solar spectrum and the IQE [11] of the simulated solar cells (bottom). The curves labeled Li are modules with structures reproduced from [9] (see Section II-B2). Reflectance is shown for light at normal incidence, except for the curve labeled Li (44°), which shows reflectance with light incident at 44° from normal. Because the Ideal reflector is behind the module's front glass surface, light can still interact with the glass and this module's reflectance is not perfect.

Module D was a real and simulated 60-cell (1.6 m²), ~15% efficient crystalline silicon module with conventional packaging materials and an aluminum frame. This module was made in 2012.

Module E was a real and simulated 36-cell (0.6 m²), ~17% efficient crystalline silicon module with conventional packaging materials and an aluminum frame. This module was made in 2016.

Module F was a real 36-cell (0.6 m²), ~11% efficient crystalline silicon module with conventional packaging materials and an aluminum frame. This module was made in the 1990s.

B. Thermal Modifications

We modified the baseline modules to implement each thermal modification. The modifications are numbered according to Table II.

1) Efficiency and Temperature Coefficient: While efficiency and temperature coefficient are not normally free parameters, we simulated their effects on operating temperature to establish the sensitivity of temperature prediction on these parameters. Using module A, we simulated increasing module efficiency by 5% (relative), from 17.1% to 18.0% (modification 1). We separately simulated halving the temperature coefficient, from -0.39 to $-0.20\% \, \text{K}^{-1}$ (modification 2).

2) Front Optical Modifications: Using module A, we simulated the addition of an ideal subbandgap reflector, reflecting 100% of the power in the solar spectrum below the cell bandgap and transmitting 100% of the power above the cell bandgap. This ideal reflector is positioned between the front glass and front encapsulant (modifications 3–5). The simulated reflectances of module A and of the module with the ideal subbandgap reflector are shown in Fig. 1. Some infrared absorption in the glass is still apparent for this modification because the ideal reflector

is at the glass/EVA interface; thus, all incident light interacts with the glass. We also simulated the addition of an ordinary antireflective coating on the glass by including 99 nm of the coating described in [8, Sec. 3.2] (modifications 4 and 6). To understand the most extreme possible performance of antireflection approaches, we modeled an ideal antireflective coating on the front glass, which achieves unity transmission at the air/glass interface (modifications 5 and 7).

We also simulated the addition of multilayer stacks that have recently been suggested in the literature for incorporation on the front surface of the module [9]. Briefly, these structures are aperiodic thin-film stacks on the front of the glass optimized to reflect subbandgap light and transmit above-bandgap light. Modification 8 is photonic cooler I and modification 9 is photonic cooler II, as reported in the supplementary information of [9]. We reproduced the reflectance curves reported in that work using refractive indexes calculated with the Brendel oscillator parameters reported elsewhere [10] and with the layer thicknesses increased 10% relative to those in [9]. This gave excellent agreement between calculated reflectance curves and those reported in [9]. Fig. 1 shows the simulated reflectance of a module featuring modification 8 with light at normal incidence and at $44°$ away from normal incidence. This illustrates an important tradeoff that must be managed in the design on these types of reflectors. The reflection band shifts to shorter wavelengths at off-normal incidence, reflecting light that is usable by the solar cell. For modifications 8 and 9, we also increased the module front surface emissivity to 0.9 to match the reported value for these coatings.

Using modules C and E, we performed outdoor testing of the effect of adding a polymer reflector film to the front surface (modifications 10, 11, and 12). In air, the film reflected 58% of the power in the AM1.5G solar spectrum between 1100 and 2500 nm and 14% from 280 to 1100 nm. We also tested a version of module E with thermal insulation on the back surface, as described in the following, with and without a reflector film.

We also considered a module containing GaAs cells (see row 13 in Table II), with unusually high subbandgap reflectivity ($>60\%$ of the subbandgap power in the solar spectrum), high efficiency ($>23\%$), and an unusually small temperature coefficient ($-0.08\% \, K^{-1}$). This module was an improved version of the one we have studied previously [12]. Over the course of a year, we compared the outdoor operating temperature and power output of this module with that of module F, which was deployed on the same testbed at the National Renewable Energy Laboratory.

3) Back Surface Reflectance: Using module C, we performed outdoor testing of the application of a high-reflectivity coating to the module's back surface (modification 14). The coating increased the hemispherical reflectance of the back surface from 44% to 89% of the power in the solar spectrum and increased the emissivity of the back surface from 0.88 to 0.93.

4) Packaging Emissivity: Using module A, we simulated increasing the emissivity of the front surface to 1.0 (modification 15), the rear surface to 1.0 (modification 16), and both front and rear surfaces to 1.0 (modification 17). Because some backsheet products contain a foil layer that decreases their emissivity, we

also simulated the reduction of the rear surface emissivity to 0.75 (modification 18).

5) Packaging Thermal Conductivity: Using module A, we simulated doubling the through-plane thermal conductivity (k) of the backsheet (modification 19). We also simulated doubling the through-plane conductivity of both the back encapsulant and the backsheet (modification 20).

Using module D, we performed outdoor testing of the effect of nearly doubling the through-plane k of the back encapsulant and backsheet materials from 0.21 to 0.41 $W \cdot m^{-1} \cdot K^{-1}$ (modification 21). This was done by comparison with a module that was otherwise identical to module D, but was originally fabricated with special back packaging materials. These materials did not contain any layers, such as metal or graphite, that would be expected to introduce strong anisotropy in heat conduction.

Using module B, we simulated the introduction of a 100-μm layer of aluminum in the backsheet (modification 22) by increasing k of the backsheet to 0.31 $W \cdot m^{-1} \cdot K^{-1}$ in the through-plane direction and 40 $W \cdot m^{-1} \cdot K^{-1}$ in the in-plane direction and reducing the backsheet emissivity to 0.75.

Using module E, we simulated and tested outdoors the addition of two layers of thermal insulation to the back surface of the module (modifications 12 and 23). The back surface of the outer layer of insulation was painted with black paint (solar absorption 0.95). This treatment was made to one module with the subbandgap reflector film and one without. While not a temperature-reduction strategy itself, the insulation served to demonstrate the subbandgap reflector film under thermally adverse conditions. These conditions mimicked those encountered in a roof-integrated application, where no convection or radiation heat transfer acts directly on the back surface of the module. Simulating the thermal insulation also served to validate the model's effectiveness for making temperature and energy predictions based on measured properties.

C. Transient Photovoltaic System Thermal Model

We simulated the operating temperature of solar cells in a PV system for up to an entire year in Golden, CO, USA, using the finite-element method [13]. This model was used for simulations of modules A, D, and E. The simulation framework is illustrated in Fig. 2. This simulation framework differs from other empirical or phenomenological models, where the objective is predicting temperature for a particular PV system based on ambient conditions. Instead, this model's objective is to predict changes in PV module temperature as a result of changes to the PV module itself. As such, it is physics based and uses almost exclusively measured material properties.

1) Geometry: We used a 2-D model of the cross section (the plane containing the "up" and "north" vectors) of a fixed-tilt PV system. The geometry of the model is shown schematically in Fig. 3. Three rows of modules were simulated, with conduction explicitly simulated in the middle module row and the surface temperatures of the front and back row constrained to match the surface temperatures of the middle module. This represented a system with infinitely many rows. Modules were modeled as a plane wall; the frame, interconnects, and gaps between cells
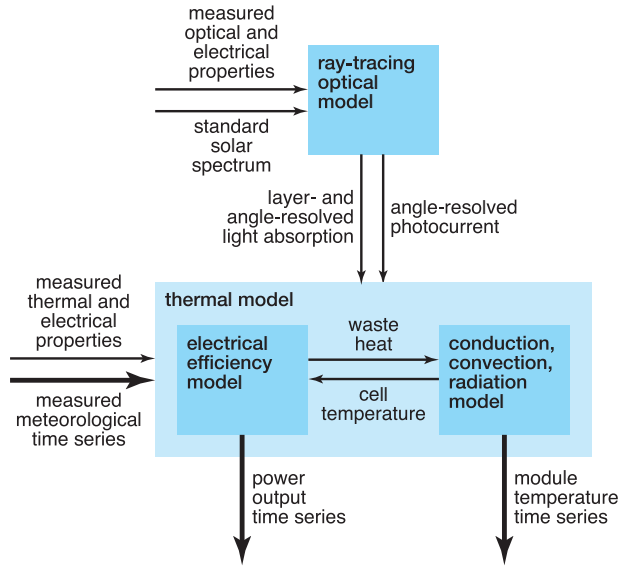
Fig. 2. Diagram illustrating our simulation approach is shown. The ray-tracing optical model is used to produce absorption and photocurrent information for the thermal model. The thermal model combines these results with meteorological time series data to simulate the coupled thermal and electrical behavior of the PV module, producing time series of simulated module temperature and electrical power.
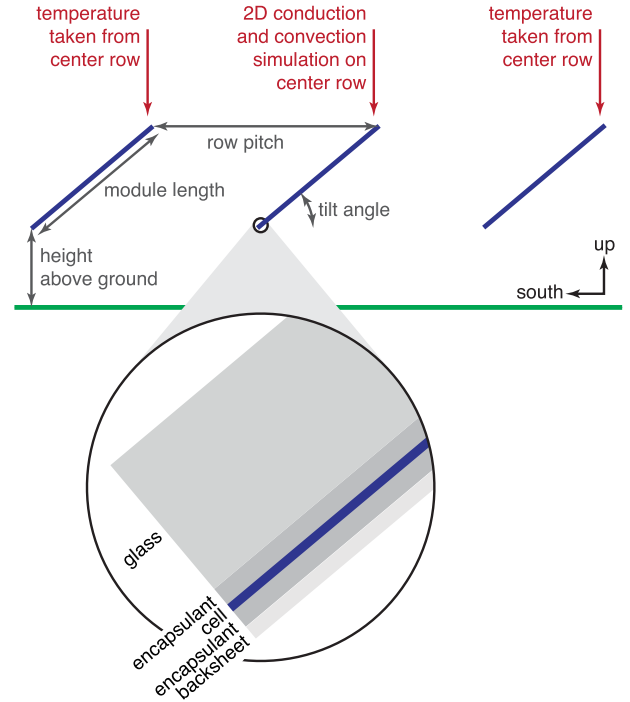

Fig. 3. Geometry used in the transient PV system thermal model is shown schematically. Two-dimensional conduction was simulated in the layers shown in the inset for the center row. The resulting surface temperatures were used for the front and back rows (for the purposes of radiative heat transfer) to simulate an infinite number of rows.

were neglected in the model geometry. Geometric parameters are summarized in Table I. Although we considered different sizes of modules, this size difference had a minor effect on simulation results. Scaling the module height and row pitch down by 50% or up by 25% resulted in a < 0.01 K change to ΔT_w. Therefore, we used the same simulation geometry in every case.

2) Optics: The heat to be delivered to each layer of the module was calculated in a spectrally resolved fashion using ray tracing that also accounts for coherent effects in thin films [14], [15]. This approach enabled the simulation of effects on various length scales, from thin-film interference to cell texturing. The incident spectrum was assumed to be proportional to the AM1.5G spectrum, and the heat absorbed in each layer was proportional to incident irradiance measured using a thermopile pyranometer tilted at $40°$. The optical simulation was carried out at $11°$ steps in angle of incidence from $0°$ to $88°$. For each incidence angle, we calculated the total energy absorbed in each module layer. We also calculated the hemispherical average for each layer's total energy absorbed; this was used to simulate the effects of the diffuse component of solar radiation. For each angle and the isotropic case, we also calculated the fractional change in photocurrent relative to the normal-incidence baseline case from the integration of the spectrally resolved absorption in the Si layer (cell), obtained from the ray-tracing simulations, multiplied by a typical c-Si internal quantum efficiency (IQE) [11]. IQE refers to the electrical collection efficiency with which photocarriers created by photons of a given wavelength are collected. The IQE does not include optical losses. We use it here as opposed to the external quantum efficiency to avoid double-counting optical losses accounted for in the ray-tracing simulations. The resulting photocurrent factor was used to modify

the module efficiency for the subsequent transient thermal simulations.

The light incident on the module's back surface was assumed to be proportional to the plane-of-array irradiance. In simulations, this energy was delivered to the module back surface according to the surface's absorptivity. The back-side irradiance fraction, derived from experimental data on our testbed, and module back surface absorptivity are shown in Table I.

3) Conduction: Heat was delivered uniformly to each layer of the thermal model according to results from the ray-tracing model. In the cell layer, the PV cell's temperature-dependent efficiency was evaluated at the cell layer's average temperature using the power temperature coefficient model [16]. This efficiency was modified by the angle-dependent factor calculated using the optical model and was used to sink the amount of energy that was converted to electricity. Material properties relevant to the conduction simulation are shown in Table I.

4) Convection: We simulated convection on the front and rear module surfaces using Newton's law of cooling. We used the convection correlation for a flat plate in parallel flow at the wind speed measured by an ultrasonic anemometer and with measured ambient temperature [17]. Because this correlation underestimates convection for PV systems, we modified it by scaling the characteristic length to match experimental data at our facility. This scale factor is the only fitting parameter in the model, and the same value (0.56) was used in every simulation in this work.

TABLE I
MATERIAL PROPERTIES AND OTHER PARAMETERS FOR THE THERMAL MODEL

parameter	material	value	units	source
emissivity	low-iron solar glass	0.88		measured
emissivity	polymer backsheet	0.87		measured
emissivity	polymer/aluminum/polymer backsheet	0.75		measured
emissivity	concrete	0.88		[17]
thermal conductivity	low-iron solar glass	1	$W \cdot m^{-1} \cdot K^{-1}$	[19]
thermal conductivity	EVA	0.26	$W \cdot m^{-1} \cdot K^{-1}$	measured
thermal conductivity	silicon solar cell	148	$W \cdot m^{-1} \cdot K^{-1}$	[20]
thermal conductivity	polymer backsheet	0.26	$W \cdot m^{-1} \cdot K^{-1}$	measured
thermal conductivity	silicone adhesive	0.2	$W \cdot m^{-1} \cdot K^{-1}$	[21]
thermal conductivity	polystyrene insulation (inner)	0.029	$W \cdot m^{-1} \cdot K^{-1}$	[22]
thermal conductivity	polyisocyanurate insulation (outer)	0.022	$W \cdot m^{-1} \cdot K^{-1}$	[23]
density	low-iron solar glass	2500	$kg \cdot m^{-3}$	[19]
density	EVA	960	$kg \cdot m^{-3}$	[24]
density	silicon solar cell	2330	$kg \cdot m^{-3}$	[25]
density	polymer backsheet	1200	$kg \cdot m^{-3}$	[25]
density	polystyrene insulation (inner)	20.8	$kg \cdot m^{-3}$	[22]
density	polyisocyanurate insulation (outer)	32	$kg \cdot m^{-3}$	[23]
specific heat	low-iron solar glass	720	$J \cdot kg^{-1} \cdot K^{-1}$	[19]
specific heat	EVA	2090	$J \cdot kg^{-1} \cdot K^{-1}$	[24]
specific heat	silicon solar cell	677	$J \cdot kg^{-1} \cdot K^{-1}$	[25]
specific heat	polymer backsheet	1250	$J \cdot kg^{-1} \cdot K^{-1}$	[25]
specific heat	polystyrene insulation (inner)	1200	$J \cdot kg^{-1} \cdot K^{-1}$	[26]
specific heat	polyisocyanurate insulation (outer)	1453	$J \cdot kg^{-1} \cdot K^{-1}$	[26]
thickness	low-iron solar glass	3.2	mm	[19]
thickness	EVA	0.4	mm	measured
thickness	silicon solar cell	0.15	mm	measured
thickness	polymer backsheet	0.3	mm	measured
thickness	polystyrene insulation (inner)	25	mm	measured
thickness	polyisocyanurate insulation (outer)	51	mm	measured
module length		1	m	
height above ground		0.5	m	
row pitch		1.53	m	
tilt		40	degrees	
azimuth		180	degrees	
back irradiance fraction		0.1		measured
back solar absorptivity		0.33		measured
plane-of-array irradiance		time series		measured
ambient temperature		time series		measured
wind speed		time series		measured
effective sky temperature		time series		measured
effective ground temperature		time series		measured

5) Radiation: We assumed the module surfaces and ground surface to be gray bodies with constant emissivity values. The ground surface was modeled as concrete. The sky was modeled as distant black surroundings with uniform temperature. Effective ground and sky temperatures were derived from long-wavelength radiation measurements from downward- and upward-facing pyrgeometers at a nearby meteorological station [18]. Areas of ground covered by the PV system's shadow were assumed to be at the ambient temperature. The view factors between surfaces in the model were calculated using the hemicube method [13].

D. Steady-State Photovoltaic Module Model With a Frame

To simulate module B and the modified version of module B (modification 22), we used a 2-D finite-element model of a PV module including a cross section of the aluminum frame bonded to the laminate with silicone adhesive. The frame and adhesive were omitted from the transient simulation for simplicity, but were required to investigate the potential for the frame to act as a cooling enhancement. We simulated steady-state conditions at $1000 \, W \cdot m^{-2}$ with radiation and convection conditions typical for this irradiance in our location. We applied an $8.2 - W \cdot m^{-2} \cdot K^{-1}$ convection coefficient with $16.9 \, °C$ surroundings on module and outer frame surfaces and radiation with uniform $14.9 \, °C$ surroundings on module front and back surfaces only. The steady-state simulation was representative of operation in high-irradiance conditions, when the potential for temperature reduction is highest and when the benefit of a temperature reduction is greatest. As such, the results were not used to predict an energy benefit, but instead to screen for whether a frame modification could be promising.

E. Outdoor Testing

For outdoor testing, modules were deployed in Golden, CO, USA, tilted at $40°$ and oriented south. *I–V* curves and module rear surface temperature measurements were collected automatically every 5 min on modules C, D, and E and every 15 min on module F and the GaAs module. Surface temperature

TABLE II
RESULTS OF THERMAL MODIFICATIONS

	modification type	variation	baseline module	ΔT_w (K) improvement	relative energy improvement total	thermal contribution	other contribution
1	efficiency increase	increase efficiency 5% (relative)	A	0.2[s]	0.054[s]	0.001[s]	0.053[s]
2	temperature coefficient decrease	decrease temperature coefficient by half	A	0.1[s]	0.023[s]	<0.001[s]	0.023[s]
3	front optical modification	ideal sub-bandgap reflector behind glass	A	3.8[s]	0.017[s]	0.016[s]	0.001[s]
4	front optical modification	ideal sub-bandgap reflector with ordinary antireflective coating	A	3.4[s]	0.038[s]	0.014[s]	0.024[s]
5	front optical modification	ideal sub-bandgap reflector with ideal antireflective coating	A	2.8[s]	0.086[s]	0.011[s]	0.074[s]
6	front optical modification	ordinary antireflective coating	A	−0.4[s]	0.022[s]	−0.002[s]	0.023[s]
7	front optical modification	ideal antireflective coating	A	−1.2[s]	0.068[s]	−0.005[s]	0.072[s]
8	front optical modification	reflector on outside surface (Li)	A	3.4[s]	0.019[s]	0.014[s]	0.005[s]
9	front optical modification	reflector on outside surface (Li omni-directional)	A	2.3[s]	0.015[s]	0.009[s]	0.006[s]
10	front optical modification	infrared reflector film on front surface	C	3[e,p]	−0.10[e,p]		
11	front optical modification	infrared reflector film on front surface	E	4[e,p]	−0.08[e,p]		
12	front optical modification	infrared reflector film on front surface with insulated back	E	−8[e,p]	−0.11[e,p]		
13	front optical modification	GaAs module	F	12[e]	0.09[e]		
14	increase back reflectance	reflective coating on back surface	C	1.7[e,p]	0.01[e,p]		
15	emissivity change	front emissivity 1.0	A	0.8[s]	0.004[s]	0.004[s]	0[s]
16	emissivity change	back emissivity 1.0	A	0.5[s]	0.002[s]	0.002[s]	0[s]
17	emissivity change	front and back emissivity 1.0	A	1.3[s]	0.006[s]	0.006[s]	0[s]
18	emissivity change	back emissivity 0.75	A	−0.5[s]	−0.002[s]	−0.002[s]	0[s]
19	thermal conductivity change	double through-plane k in backsheet	A	0.1[s]	<0.001[s]	<0.001[s]	0[s]
20	thermal conductivity change	double through-plane k in backsheet and back encapsulant	A	0.1[s]	0.001[s]	0.001[s]	0[s]
21	thermal conductivity change	isotropic 1.95× increase in backsheet and encapsulant k	D	0.1[s] <1[e]	<0.01[s] <0.01[e]		
22	thermal conductivity change	addition of 100-μm aluminum film in backsheet	B	0.2[s,t]	<0.01[s,t]		
23	thermal conductivity change	insulated back	E	−13[s,p] −12[e,p]	−0.05[s,p] −0.06[e,p]		

Simulation and experimental results are shown for each thermal modification. Each case is compared to a baseline module described in Section II-A. The improvement in ΔT_w is shown, where a positive value results from a reduction in operating temperature. The fractional improvement in energy production is shown, where a positive value results from an increase in energy production. For simulations, the energy improvement is decomposed into thermal and other contributions as explained in Section II. Superscript "s" refers to simulation results and superscript "e" refers to experimental results. Superscript "p" refers to a partial-year experiment or simulation and superscript "t" refers to a steady-state simulation.

measurements were made with thin type-T thermocouples adhered to module surfaces using a polyester tape.

The outdoor testbed was equipped with thermopile pyranometers. To eliminate temperature inaccuracy introduced by adding the reflective coating to module C between the temperature probe and the module's back surface, we derived cell temperature from irradiance and V_{oc} for module C.

The GaAs module and module F were deployed together for one year, and we used their back surface temperatures assuming like packaging materials in each module.

III. RESULTS AND DISCUSSION

Sample output of the thermal model is compared with outdoor measurements for module E and the thermally insulated version of module E (modification 23) in Fig. 4. The simulation shows good agreement with the experiment over a range of conditions; however, the simulated temperature is slightly biased above the experiment under high-temperature conditions and below the experiment under low-temperature conditions. The thermal model has only a single fitting parameter, the characteristic
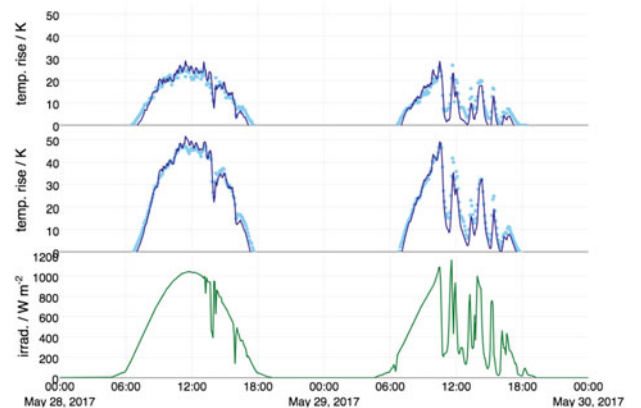

Fig. 4. Temperature rise above ambient for module E (top plot) and the insulated-back version of module E (middle plot). Outdoor measurements are shown as points and simulation results as a solid line, demonstrating good agreement for a range of conditions. Plane-of-array irradiance is shown in the bottom plot.

length scaling factor for convection heat transfer, and this parameter was fitted using experimental data from a different PV system during a different time period. There is disagreement
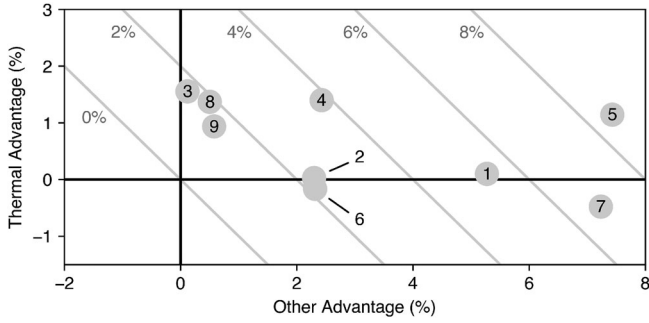
Fig. 5. Energy advantage of several of the module modifications is decomposed into "thermal" and "other" components. The numbers refer to the modifications listed in Table II. The diagonal lines show contours of equal total advantage.

about the appropriate functional form for convection heat transfer in PV [27]. The available relationships use parameters that may require refitting according to system-specific features or geographic location [28]. To keep the model a mainly physics-based prediction tool rather than a fitted model, we chose a very simple convection relationship, which does not include free convection. Our results are, thus, a compromise between model accuracy and the number of fitting parameters. There may be cases, such as locations where free convection dominates over forced convection, where a more complex convection function would be required. The sample data and the comparisons between simulation (superscript "s") and experiment (superscript "e") shown in rows 21 and 23 of Table II demonstrate that the thermal model can make good predictions based only on measured properties.

Results from the thermal modifications are summarized in Table II and discussed in detail in the following. Results are given as differences in ΔT_w or fractional difference in E_{DC} between the indicated baseline module and the module with the change described in the "variation" column. A positive value indicates an improvement, either a temperature reduction or an energy increase. Values for simulation (superscript "s") and experiment (superscript "e") are given where available. Results from partial-year simulations and experiments (superscript "p") may not represent full-year performance due to seasonal effects. The steady-state simulation is marked with superscript "t." Where a "<" symbol is present, it shows that the result was between zero and the indicated value. The "thermal" and "other" components of energy benefit are illustrated for a subset of the modifications in Fig. 5.

A. Efficiency and Temperature Coefficient

We considered the effects of efficiency and temperature coefficient improvement for easy comparison to the other thermal modifications. The results are shown in Table II and Fig. 5. Improving efficiency from 17.1% to 18% (modification 1) or halving of the temperature coefficient (modification 2) each only reduced the production of waste heat in the cell by about 1%, giving a small effect on operating temperature. While these changes result in major improvements to energy production, they do not cause major temperature reductions.

B. Front Optical Modifications

The results from the addition of an ideal subbandgap reflector (modification 3) are shown in Table II and Fig. 5. The ideal reflector gave a substantial temperature reduction. Considering only high-irradiance conditions, this reduction approached 5 K, consistent with previous results [29].

Table II and Fig. 5 also show results from combinations of antireflective coatings and subbandgap reflective coatings (modifications 4–7) illustrating the competing effects of increasing energy conversion using antireflection and decreasing temperature using subbandgap reflection. Adding an antireflective coating alone reduces the module's subbandgap reflectivity and raises its temperature (modifications 6 and 7). Our results show that adding a subbandgap reflector (modifications 4 and 5) can counteract this effect and further improve energy gain.

A comparison of the results of the ideal subbandgap reflector (modification 3) and the ideal antireflection coating (modification 7) indicates that there is substantially more photocurrent gain than thermal improvement to be realized through front optical modifications. However, the 1.6% improvement in energy yield available (for this particular simulated PV system and location) with the subbandgap reflector is appreciable. It is also important to note that infrared performance of antireflection approaches should be considered. As shown in Table II and Fig. 5, introducing the ideal antireflection coating has detrimental thermal effect, which should be considered and managed in the design of such coatings.

Results from simulations of the multilayer stack proposed by Li (modifications 8 and 9) shown in Table II and Fig. 5 indicate that both coatings realize an operating temperature reduction. The omnidirectional version of the coating (modification 9) trades a reduced thermal benefit for a small benefit in above-bandgap performance. It is important to note that this is not a universal result; it depends on the location (i.e., weather and irradiance) and configuration of the PV system. However, it highlights an important challenge with thin-film stack reflectors that reflection bands shift to shorter wavelengths at off-normal incidence. Thus, a balance must be struck between the position of the short-wavelength edge of the normal-incidence reflection band and the off-angle transmission above the solar cell's bandgap. The difference in performance between modification 8 and 9 in this particular fixed-tilt application illustrates this tradeoff.

Outdoor tests of the polymer reflector film (modifications 10 and 11) showed a substantial temperature benefit. However, because the filter reflected a portion of the solar spectrum's power above the cell's bandgap, the treatment resulted in a current reduction that caused a loss in energy. We anticipate that this film would have better performance inside the module due to the elimination of the reflective interface between the film and air. We attribute the small discrepancy in performance between modifications 10 and 11 to the different weather (including spectrum, irradiance, angle of incidence, and temperature) during the two partial-year tests and the different spectral and angular responses of the modules. Comparing the insulated-back module (modification 23) with the insulated-back module with infrared

reflector film (modification 12) shows a greater thermal benefit than application of the film to an open-back module (about a 5 K temperature decrease). This illustrates that the strategy of reducing the amount of waste heat produced in the module gives a thermal benefit that becomes larger when the removal of heat from the module is compromised.

The GaAs module's (see row 13 in Table II) high subbandgap reflectivity, small temperature coefficient, and high efficiency gave it a major temperature advantage compared with module F. Compared with module F, the GaAs module had a smaller form factor, lacked a frame, and was mounted in a different location on the same rack. These factors may have caused differences in convective cooling that would appear in the temperature improvement metric. Details about the thermal, optical, and electrical performance of this module type are described in our previous work [12]. The energy advantage shown for GaAs is normalized for the difference between the module's STC performance and the control module's STC performance; therefore, it is corrected for the first-order effects of differences in area and efficiency. Assuming a temperature coefficient of $-0.5\%\,\mathrm{K}^{-1}$ for module F, manufactured in the 1990s, we determined that of the 9% normalized energy benefit of the GaAs module, approximately 7% is due to low operating temperature and 2% is due to small temperature coefficient.

C. Back Surface Reflectance

Adding a reflective coating to reject light incident on module C's back surface (modification 14) yielded a substantial temperature decrease. This treatment is promising because it may be simpler to engineer a weatherproof broadband reflective coating than a selective reflector with high transmission of light usable to the cell. This modification applies to modules, like CIGS and CdTe, that normally have a low-reflectivity back surface.

D. Packaging Emissivity

Unlike the emissivity of bare silicon or metal, the emissivity of PV module packaging materials is relatively high. Further increasing the emissivity of only one surface (modifications 15 and 16) had a modest effect, consistent with previous results [29], [30]. Increasing both outside surface emissivity values (modification 17) gave a larger effect, but provided less than a 1% increase in energy output. Reducing emissivity by using a backsheet containing an aluminum layer (modification 18) resulted in a small temperature increase due to poorer radiation heat transfer. In an opaque backsheet material, increasing emissivity without increasing absorption of sunlight is possible. However, it may be difficult to produce a low-cost weatherproof coating for glass that increases the module's front emissivity.

E. Packaging Thermal Conductivity

Because it is relatively thin and the energy flux density across it is relatively small, the through-plane thermal resistance of PV packaging materials is relatively low. Reducing this thermal resistance further (modifications 19 and 20) had a very small effect in simulations.

Increasing the k of back packaging can cause the module back surface temperature to increase even if the cell temperature has decreased. In outdoor testing of the module with high-thermal-conductivity back packaging (modification 21), we detected a difference in surface temperature small enough that we could not conclude that there was a substantial reduction in cell temperature. A simulation of the same test matched this result.

An aluminum frame acts as a surface area enhancement and, combined with a backsheet having high in-plane k (modification 22), increases removal of heat at the module edges. Our simulation predicted the maximum benefit, occurring in sunny conditions and with unobstructed convection on the outer surfaces of the module frame. Adding a foil layer cooled the cell adjacent to the frame by 0.7 K but reduced radiative heat transfer due to the metal-containing backsheet led to a net temperature increase.

Adding insulation to the module back surface (modification 23) caused a major increase in operating temperature and reduction in energy production. The simulation was a satisfactory match to the experiment and shows the disadvantage of mounting configurations with limited heat transfer from the module back surface.

F. Extension of Module Service Life

While it is impossible to explicitly predict the service life of a PV module, among the module's many parallel and serial degradation mechanisms are several that are thermally activated. A rough approximation of overall degradation is possible by using the Arrhenius equation to model degradation as a single thermally activated process. We calculated time to failure TF as

$$\mathrm{TF} = \frac{1}{\sum_t A\Delta t \exp \frac{-E_a}{k_b T}}$$

where E_a is activation energy, k_b is the Boltzmann constant, T is module temperature, Δt is the simulation time step, and the denominator is summed over all time steps of the thermal simulation. Because we make only relative comparisons of TF, the value of the preexponential factor A is arbitrary. There is not a well-established activation energy for the overall degradation process, but we can make a crude assessment of the lifetime extension offered by temperature reduction by assuming a range of effective activation energy values from 0.6 to 2 eV [2]. Under these simple approximations, the ideal subbandgap reflector can yield an increase in TF ranging from 26% to 200%. This is a major simplification that neglects the effects of moisture, ultraviolet light, mechanical stress, other driving forces for failure, and the interactions among concurrent failure mechanisms. However, we use the result to illustrate that temperature reduction can have a role beyond improved energy production.

IV. Conclusion

PV module temperature can be reduced through reductions in waste heat generation or improvements in waste heat rejection. We found that strategies reducing waste heat generation generally performed better than those improving waste heat rejection. Changes to thermal conductivity and back emissivity yielded only modest temperature changes. Strategies reducing

the irradiance-weighted temperature rise of PV modules by more than 1 K included rejecting subbandgap light from the module or cell, reflecting light from the module back surface, and giving both front and back surfaces ideal emissivity. Optical modifications that alter the module's reflection of light must balance their thermal effects with nonthermal optical effects to maximize the production of energy.

References

[1] J. Nelson, *The Physics of Solar Cells*. London, U.K.: Imperial College Press, 2003.

[2] S. Kurtz *et al.*, "Evaluation of high-temperature exposure of photovoltaic modules," *Prog. Photovolt., Res. Appl.*, vol. 19, no. 8, pp. 954–965, 2011.

[3] M. Hasanuzzaman, A. Malek, M. Islam, A. Pandey, and N. Rahim, "Global advancement of cooling technologies for PV systems: A review," *Sol. Energy*, vol. 137, pp. 25–45, 2016.

[4] S. Sargunanathan, A. Elango, and S. T. Mohideen, "Performance enhancement of solar photovoltaic cells using effective cooling methods: A review," *Renewable Sustain. Energy Rev.*, vol. 64, pp. 382–393, 2016.

[5] J. Siecker, K. Kusakana, and B. Numbi, "A review of solar photovoltaic systems cooling technologies," *Renewable Sustain. Energy Rev.*, vol. 79, pp. 192–203, 2017.

[6] A. Shukla, K. Kant, A. Sharma, and P. H. Biwole, "Cooling methodologies of photovoltaic module for enhancing electrical efficiency: A review," *Sol. Energy Mater. Sol. Cells*, vol. 160, pp. 275–286, 2017.

[7] M. R. Vogt *et al.*, "Reduced module operating temperature and increased yield of modules with PERC instead of Al-BSF solar cells," *IEEE J. Photovolt.*, vol. 7, no. 1, pp. 44–50, Jan. 2017.

[8] M. R. Vogt, "Development of physical models for the simulation of optical properties of solar cell modules," Ph.D. dissertation, Faculty Math. Phys., Gottfried Wilhelm Leibniz Univ. Hannover, Hannover, Germany, 2015.

[9] W. Li, Y. Shi, K. Chen, L. Zhu, and S. Fan, "A comprehensive photonic approach for solar cell cooling," *ACS Photon.*, vol. 4, no. 4, pp. 774–782, 2017.

[10] J. Kischkat *et al.*, "Mid-infrared optical properties of thin films of aluminum oxide, titanium dioxide, silicon dioxide, aluminum nitride, and silicon nitride," *Appl. Opt.*, vol. 51, no. 28, pp. 6789–6798, Oct. 2012.

[11] C. Tool *et al.*, "17% mc-Si solar cell efficiency using full in-line processing with improved texturing and screen-printed contacts on high-ohmic emitters," in *Proc. 20th Eur. Photovolt. Sol. Energy Conf. Exhib.*, 2005, vol. 6, p. 10.

[12] T. J. Silverman *et al.*, "Outdoor performance of a thin-film gallium-arsenide photovoltaic module," in *Proc. 39th IEEE Photovolt. Spec. Conf.*, 2013, pp. 103–108.

[13] *COMSOL Heat Transfer Module User's Guide*, COMSOL, Los Angeles, CA, USA, 2017.

[14] I. Subedi, T. J. Silverman, M. Deceglie, and N. J. Podraza, "Impact of infrared optical properties on crystalline Si and thin film CdTe solar cells," in *Proc. 44th IEEE Photovolt. Spec. Conf.*, 2017.

[15] I. Subedi, T. J. Silverman, M. Deceglie, and N. J. Podraza, "Al+Si interface optical properties obtained in the Si solar cell configuration," *Phys. Status Solidi A, Appl. Mater. Sci.*, vol. 214, no. 12, 2017, Art. no. 1700480.

[16] B. Marion, "Comparison of predictive models for photovoltaic module performance," in *Proc. 33rd IEEE Photovolt. Spec. Conf.*, 2008, pp. 1–6.

[17] F. P. Incropera and D. P. DeWitt, *Fundamentals of Heat and Mass Transfer*, 5th ed. Hoboken, NJ, USA: Wiley, 2002.

[18] A. Andreas and T. Stoffel, "NREL solar radiation research laboratory (SRRL): Baseline measurement system (BMS)," Nat. Renewable Energy Lab., Golden, CO, USA, Tech. Rep. DA-5500-56488, 1981.

[19] *Solite Patterned Glass Datasheet*, AGC Solar, Kingsport, TN, USA, 2012.

[20] Z. Lu and Q. Yao, "Energy analysis of silicon solar cell modules based on an optical model for arbitrary layers," *Sol. Energy*, vol. 81, no. 5, pp. 636–647, 2007.

[21] *Silicon-Based Photovolt. Solutions*, Dow Corning, Auburn, MI, USA, 2015.

[22] *Foamular Extruded Polystyrene Insulation Datasheet*, Owens Corning, Toledo, OH, USA, 2011.

[23] *Thermasheath-3 Insulation for the Building Envelope*, Rmax Operating, Dallas, TX, USA, 2015.

[24] *Photocap Solar Cell Encapsulants Technical Manual*, Specialized Technology Resources, Enfield, CT, USA, 2015.

[25] A. Jones and C. Underwood, "A thermal model for photovoltaic systems," *Sol. Energy*, vol. 70, no. 4, pp. 349–359, 2001.

[26] *Isolparma Thermal Insulation Boards Datasheet*, Isolparma Srl, Padova, Italy, 2007.

[27] E. Skoplaki and J. Palyvos, "Operating temperature of photovoltaic modules: A survey of pertinent correlations," *Renewable Energy*, vol. 34, no. 1, pp. 23–29, 2009.

[28] E. Barykina and A. Hammer, "Modeling of photovoltaic module temperature using Faiman model: Sensitivity analysis for different climates," *Sol. Energy*, vol. 146, pp. 401–416, 2017.

[29] X. Sun *et al.*, "An optics-based approach to thermal management of photovoltaics: Selective-spectral and radiative cooling," *IEEE J. Photovolt.*, vol. 7, no. 2, pp. 566–574, Mar. 2017.

[30] A. Gentle and G. Smith, "Is enhanced radiative cooling of solar cell modules worth pursuing?" *Sol. Energy Mater. Sol. Cells*, vol. 150, pp. 39–42, 2016.

Authors' photographs and biographies not available at the time of publication.